

# Assessment of filtered cameras for quantitative 2D analysis of divertor conditions during detachment in JET L-mode plasmas

J. Karhunen<sup>1,2</sup>, B. Lomanowski<sup>3</sup>, V. Solokha<sup>2</sup>, S. Aleiferis<sup>4</sup>, P. Carvalho<sup>5</sup>, M. Groth<sup>2</sup>, K.D. Lawson<sup>6</sup>, A.G. Meigs<sup>6</sup>, A. Shaw<sup>6</sup> and JET Contributors\*

<sup>1</sup>Department of Physics, University of Helsinki, 00014 Helsinki, Finland

<sup>2</sup>Aalto University, Department of Applied Physics, 02150 Espoo, Finland

<sup>3</sup>Oak Ridge National Laboratory, Oak Ridge, TN 37831, USA

<sup>4</sup>Institute of Nuclear and Radiological Sciences and Technology, Energy and Safety, National Center for Scientific Research 'Demokritos', Athens, 15310, Greece

<sup>5</sup>Instituto de Plasmas e Fusão Nuclear, Instituto Superior Técnico, 1049-001 Lisboa, Portugal

<sup>6</sup>CCFE, Culham Science Centre, Abingdon, OX14 3DB, UK

\*See the author list of E. Joffrin et al., Nuclear Fusion 59 (2019) 112021

**Abstract.** Estimates for 2D distributions of electron temperature,  $T_e$ , electron density,  $n_e$ , and atomic deuterium density,  $n_0$ , in the JET divertor volume have been inferred from deuterium Balmer line intensity ratios obtained from tomographic reconstructions of divertor camera measurements. This enables also investigation of ionization,  $S_{\text{ion}}$ , and recombination,  $S_{\text{rec}}$ , rates. The analysis shows a decrease of  $T_e$  to 0.5 – 1.0 eV throughout the outer divertor during detachment in low-confinement (L-mode) plasmas. Simultaneously, the high- $n_e$  region and the  $n_0$  distribution in the outer divertor are observed to elongate and shift from the outer strike point towards the X-point. The observations are in qualitative agreement and follow the same sequence with modelling predictions of EDGE2D-EIRENE simulations of a density scan. While the method was found to provide good representation of the evolution of volumetric recombination during detachment, in agreement with the simulations, the movement of the ionization front upstream could not be followed due to lack of spatial overlap between the ionization region and the necessary emission distributions. Consequently, the representation of the ionization conditions and the particle balance in the detached outer divertor are compromised. Further studies are still required to address the effects of Lyman opacity and molecular processes on the validity of the method.

## 1. Introduction

Detachment of the divertor is a direct consequence of the evolution of the electron temperature,  $T_e$ , electron density,  $n_e$ , and atomic deuterium density,  $n_0$ , and their role in radiative power losses and volumetric recombination in the divertor plasma volume [1, and therein]. The ability to measure these quantities is a key factor in the interpretation of the experimentally observed plasma conditions and explanation of the physical phenomena leading to detachment in divertor plasma simulations.

Line-integrated spectroscopic measurements of the divertor  $n_e$  and  $T_e$ , based on the Stark broadening of the high-excitation Balmer lines of deuterium [2, 3, 4] and spectral features of the continuum emission [5, 6] have become standard passive methods for studying divertor conditions in different tokamaks, such as JET [2, 4, 6], ASDEX Upgrade [3, 7] and TCV [8]. Such measurements provide critical reference data for post-processed divertor simulations but potentially misinterpret the local conditions at, e.g., the strike-point or X-point regions due to line-integration effects with spatially extended emission regions [6, 9]. Moreover, the line-integrated measurements can be prone to the effect of reflections from metallic wall surfaces [10, 11].

Several tokamaks [12, 13, 14, 15, 16, 17, 18, 19, 20, 21, 22, 23, 24, 25, 26] utilize filtered divertor camera systems and tomographic reconstructions of their images for localized 2D investigation of the divertor emission in the  $(R, z)$  plane. Such information on the 2D emission distributions is a critical reference for interpreting the plasma conditions by divertor modelling. However, utilizing the camera data directly for resolving the plasma conditions experimentally has been a less common practice and concentrated primarily on indirect identification of low-temperature regions based on relative increase of the intensities of recombination-dominated deuterium Balmer lines [16, 27, 28, 5, 29, 30, 31, 32].

More recently, more direct approaches have been taken by coupling camera analysis of 2D Balmer line intensity ratios to line-integrated spectroscopic  $n_e$  and  $T_e$  measurements for estimation of the local divertor  $n_0$  and  $T_e$  in ASDEX Upgrade [33], as well as the divertor  $n_e$ , and  $T_e$  in JET [9]. Camera observations of the line emission distributions have also been integrated into a sophisticated Bayesian multi-diagnostics method

for resolving divertor plasma conditions in 2D in the upcoming experimental campaigns of MAST Upgrade [34].

In this work, the methodology introduced in [9] has been applied for characterising the 2D spatial evolution of the divertor conditions in JET during the process of outer divertor detachment in L mode, expanding the analysis from  $n_e$  and  $T_e$  to  $n_0$ . These estimates have also been used for further analysis of the evolution of the ionization and recombination rates in the divertor volume. The applicability of the analysis method has been assessed by comparing the findings qualitatively to modelling predictions, given by an EDGE2D-EIRENE [35, 36, 37] density scan.

## 2. 2D analysis of divertor conditions with filtered cameras

Estimates for the 2D distributions of the divertor electron temperature,  $T_e$ , electron density,  $n_e$ , and atomic neutral deuterium density,  $n_0$ , are derived from intensity ratios of 2D tomographic reconstructions of the deuterium Balmer emission lines using methodology introduced in [9]. This enables also analysis of the ionization,  $S_{\text{ion}}$ , and recombination,  $S_{\text{rec}}$ , rates with the help of the ADAS database [38].

### 2.1. Tomographic reconstructions of divertor camera images

The JET divertor is observed tangentially by a dedicated camera system (KL11) [14], consisting of four cameras with near identical views, as shown in figure 1. Each of the cameras is equipped with remotely controlled filter wheels carrying selections of narrow bandpass filters suitable for observing visible-range emission of the different deuterium Balmer emission lines and various impurity species. The camera images are calibrated to absolute units of intensity with the help of the in-vessel calibration light source (ICLS) setup of JET [39, 40, 41].

Tomographic reconstructions of the divertor camera images provide 2D emission distributions in the poloidal plane across the divertor volume. The reconstructions are generated with the methodology presented in [11], which considers the reflections from the metallic wall surfaces, as described in [42]. To improve the spatial consistency between the images from the different cameras and the geometry

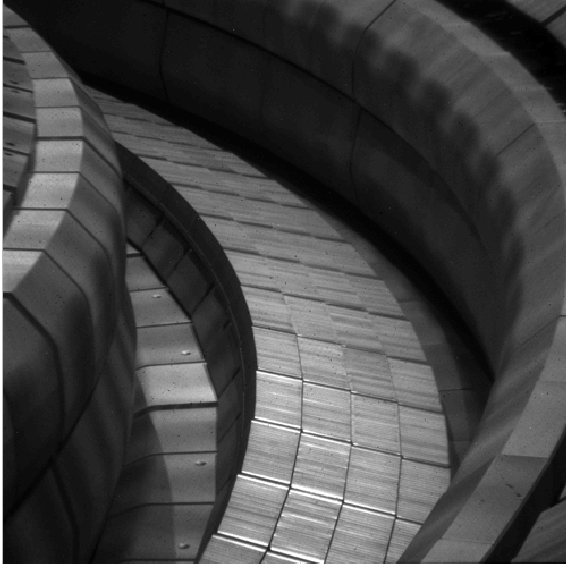


**Figure 1.** The JET divertor is observed tangentially by four filtered visible-range cameras. Image courtesy of G. Arnoux.

calibration used for tomography, a recently introduced alignment correction feature of the Calcam spatial calibration software [43] is applied during the process.

## 2.2. Estimation of $n_e$ , $T_e$ and $n_0$ from Balmer line ratios

The effect of  $T_e$ ,  $n_e$  and  $n_0$  on the line emission intensity of atomic deuterium can be investigated with the help of the collisional-radiative model by considering the origins of the emission as a combination of excitation of deuterium atoms and recombination of deuterium ions. For an electronic transition between upper and lower energy states with principal quantum numbers  $p$  and  $q$ , respectively, the emission intensity is given by

$$\begin{aligned}
 I_{p \rightarrow q} &= \frac{1}{4\pi} \left[ \underbrace{n_0 n_e PEC_{p \rightarrow q}^{\text{exc}}(n_e, T_e)}_{\text{excitation}} \right. \\
 &\quad \left. + \underbrace{n_i n_e PEC_{p \rightarrow q}^{\text{rec}}(n_e, T_e)}_{\text{recombination}} \right] \\
 &\approx \frac{1}{4\pi} [n_0 n_e PEC_{p \rightarrow q}^{\text{exc}}(n_e, T_e) \\
 &\quad + n_e^2 PEC_{p \rightarrow q}^{\text{rec}}(n_e, T_e)]. \quad (1)
 \end{aligned}$$

The photon emission coefficients,  $PEC_{p \rightarrow q}^{\text{exc/rec}}(n_e, T_e)$ , describe the  $T_e$  and  $n_e$  dependencies of the emitting excitation state populations due to excitation and recombination processes and are provided by the ADAS database. An approximation of equal electron

and ion densities,  $n_i \approx n_e$ , has been made in the recombination component to reduce the number of unknown variables, restricting the analysis to fairly pure deuterium plasmas with the effective charge state,  $Z_{\text{eff}}$ , close to unity.

Utilizing the capability of the JET divertor camera system for simultaneous observation of the deuterium Balmer lines  $D_\alpha$  ( $p = 3 \rightarrow q = 2$ , 656.1 nm),  $D_\gamma$  ( $p = 5 \rightarrow q = 2$ , 433.9 nm) and  $D_\epsilon$  ( $p = 7 \rightarrow q = 2$ , 393.9 nm), methodology for solving 2D estimates of  $T_e$ ,  $n_e$  and  $n_0$  based on the intensity ratios  $I_\alpha/I_\epsilon$  and  $I_\gamma/I_\epsilon$  of the respective tomographic reconstructions was introduced in [9]. A Markov chain Monte Carlo (MCMC) [44, 45] model was generated for solving the non-analytic optimization problem

$$\begin{aligned}
 &(PEC_\gamma^{\text{exc}} PEC_\epsilon^{\text{rec}} - PEC_\gamma^{\text{rec}} PEC_\epsilon^{\text{exc}}) \frac{I_\alpha}{I_\epsilon} \\
 &+ (PEC_\alpha^{\text{exc}} PEC_\epsilon^{\text{rec}} - PEC_\alpha^{\text{rec}} PEC_\epsilon^{\text{exc}}) \frac{I_\gamma}{I_\epsilon} \\
 &+ PEC_\alpha^{\text{exc}} PEC_\gamma^{\text{rec}} - PEC_\alpha^{\text{rec}} PEC_\gamma^{\text{exc}} = 0, \quad (2)
 \end{aligned}$$

derived from equation (1), individually in each cell of the tomography grid. Estimates for  $T_e$  and  $n_e$  are provided by the solution of equation (2) due to the implicit dependencies of the  $PEC$ s. When also the  $I_\alpha/I_\epsilon$  and  $I_\gamma/I_\epsilon$  intensity ratios are subsequently optimized with the help of equation (1) against the experimental values, an estimate for  $n_0$  is obtained. The estimates are characterized by statistical error bars of approximately 25%. For improved accuracy and robustness, the solutions for  $T_e$  and  $n_e$  are constrained by line-integrated spectroscopic  $T_e$  and  $n_e$  measurements, obtained with the vertical divertor spectroscopy set-up of JET [46, 47]. For further description and benchmark of the method, the reader is referred to [9].

## 2.3. Calculation of $S_{\text{ion}}$ and $S_{\text{rec}}$

Given estimates for  $T_e$ ,  $n_e$  and  $n_0$ , the ionization and recombination rates can be directly calculated as

$$S_{\text{ion}} = n_0 n_e SCD(n_e, T_e) \quad (3)$$

and

$$\begin{aligned}
 S_{\text{rec}} &= n_i n_e ACD(n_e, T_e) \\
 &\approx n_e^2 ACD(n_e, T_e), \quad (4)
 \end{aligned}$$

respectively. Here,  $SCD(n_e, T_e)$  and  $ACD(n_e, T_e)$  are the ionization and recombination rate coefficients, respectively, given by the ADAS database. In the case of  $S_{\text{rec}}$ , the same approximation of  $n_i \approx n_e$  has been made as for equation (1).

Calculating  $S_{\text{ion}}$  with equation (3) is more suitable for studies in detached conditions than the method based on the  $D_\alpha$  intensity used in [6] in the absence of a  $n_0$  measurement. This is due to

the increasing recombination component of the  $D_\alpha$  emission dominating over the excitation component at low temperatures, leading to strong overestimation of  $S_{\text{ion}}$  calculated from the  $D_\alpha$  intensity, as described in [6]. However, the use of equation (3) may also suffer from  $D_\alpha$ -based issues with the  $n_0$  estimate, as discussed below.

#### 2.4. Physical restrictions of the method

The spatial extent of the methodology used in this work is restricted by the Balmer line emission distributions in the divertor volume. The method is thus not capable of providing such wide spatial coverage as, e.g., the direct measurements of  $n_e$  and  $T_e$  by the divertor Thomson scattering system at DIII-D [48, 49, 50]. Furthermore, the reliance on the strongly recombination-dominated  $D_\varepsilon$  emission constrains the applicability of the method to plasma conditions with notable emission contribution from recombination. Consequently, the methodology is primarily suited for high-recycling and detached divertor conditions at low temperatures below 3 eV, whereas the lack of strong  $D_\varepsilon$  emission complicates the analysis in attached conditions with high divertor temperatures above 10 – 20 eV.

The ADAS collisional-radiative model assumes the plasma to be optically thin, which is a valid approximation in the case of the Balmer lines [51]. However, strong re-absorption of the deuterium Lyman line emission ( $p \rightarrow 1$ ) in high-recycling and detached divertor conditions has been observed in JET-ILW experiments [6], as well as in simulations for ITER [52, 53, 54]. The absorption of the photons repopulates the low excitation states contributing to Balmer line emission, consequently increasing the Balmer line intensities from the predictions of the ADAS PECs [6, 55]. Due to the re-population of the excited states, also the ionization and recombination rate coefficients are expected to be higher and lower, respectively, than the optically thin ADAS SCDs and ACDs [6]. While the effect of the Lyman series opacity cannot be properly accounted for in the methodology presented in this work, it is believed to be attenuated by the treatment of the Balmer line ratios instead of absolute line intensities.

Equation (1) considers emission arising from interactions between electrons, atoms and ions but discards molecular processes. The role of molecular interactions in excitation of deuterium atoms has, however, been suggested to lead to a noticeable additional contribution to the divertor Balmer line emission in earlier experiments and modelling work [29, 56, 57, 58, 59]. As resolved experimentally in [59], the molecular effect on the Balmer emission has been observed primarily as amplification of the

$D_\alpha$  emission with less emphasis on the  $D_\gamma$  and  $D_\varepsilon$  intensities in low-temperature recombining plasma conditions. In this work, the possible significance of the molecular processes is postulated to appear as overestimation of  $n_0$ .  $T_e$  and  $n_e$  are believed to be less affected due to the constraints imposed upon them in the optimization model with the help of the line-integrated spectroscopic measurements, as described in [9], whereas the  $n_0$  estimate could not be similarly constrained. Furthermore, due to the lesser contribution of the excitation component of equation (1) in  $D_\gamma$  and  $D_\varepsilon$  emissions, the primary involvement of  $n_0$  in the analysis comes from the  $D_\alpha$  emission which is the most affected by the molecular processes.

Both Lyman opacity and molecular processes become more prominent in low-temperature detached conditions with high atomic densities in the divertor. Simultaneously, these are the conditions in which the described methodology is applicable due to its dependence on the recombination-dominated  $D_\varepsilon$  emission, leaving the validity of the basic assumptions behind the applied model compromised. Resolving the significance of the omission of Lyman opacity and molecular processes in the analysis requires dedicated investigation with the help of modelling and experimental methods, such as that described in [59]. This is not attempted as part of this work but will be reported elsewhere.

### 3. Experimental and simulation set-up

The evolution of the outer divertor conditions during the course of detachment were studied experimentally in a density scan in JET low-confinement mode (L-mode) plasmas. To assess the credibility of the outcome of the analysis, the observed trends were compared qualitatively to the output of an EDGE2D-EIRENE density scan.

#### 3.1. JET L-mode density scan

The analysis was performed on a density scan consisting of three unseeded L-mode pulses 94759, 94771 and 94773. Each of the pulses had plasma current and toroidal magnetic field of  $I_p = -2.45$  MA and  $B_\Phi = 2.45$  T, respectively, and neutral beam heating power of  $P_{\text{NBI}} = 1.0$  MW. As illustrated in figure 2a, 94759 was a density ramp with the line-integrated edge density at the outer midplane, given by interferometry, ranging within  $n_{e,\text{edge}} \approx 2.5 - 5.1 \times 10^{19} \text{ m}^{-3}$ , while 94771 and 94773 had two density steps at approximately  $2.5 \times 10^{19} \text{ m}^{-3}$  and  $3.7 \times 10^{19} \text{ m}^{-3}$  (94771) or  $4.3 \times 10^{19} \text{ m}^{-3}$  (94773). Due to the varying plasma density, the Ohmic heating power ranged within 1.6 – 2.2 MW during the density scan.

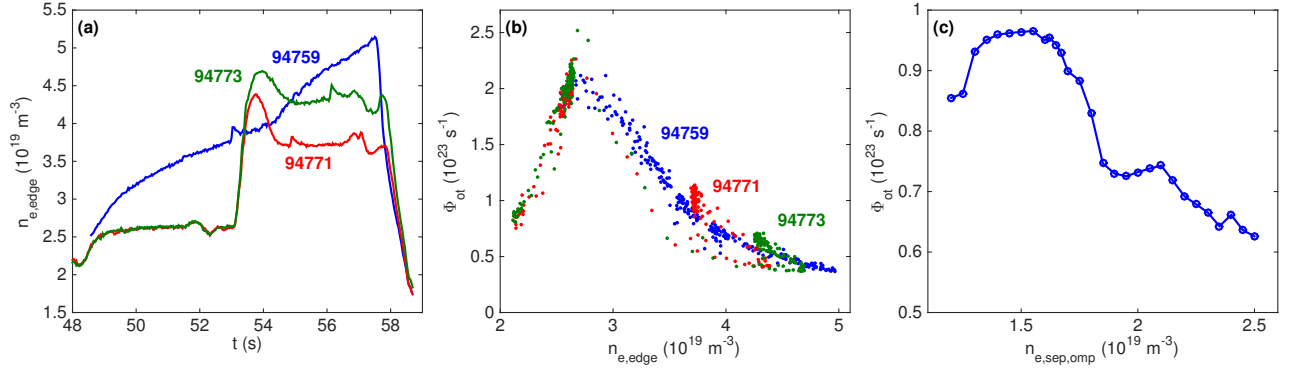


**Figure 2.** Divertor conditions were studied experimentally in JET L-mode plasmas during a density ramp pulse 94759 (blue) and two density plateau pulses 94771 (red) and 94773 (green) (a), comprising a density scan over which the outer divertor ranged from high-recycling to detached conditions (b). The line-integrated upstream edge density,  $n_{e,edge}$  in (a) is given by interferometry in the pedestal region at the outer midplane, while the total outer target ion current,  $\Phi_{ot}$ , in (b) is obtained by integrating the Langmuir probe measurements of the ion flux over the outer target plate. Qualitative comparisons were made to an EDGE2D-EIRENE density scan in which the outer divertor also ranged from high-recycling to detached conditions (c), albeit not reaching as deep detachment as in the experiment. Note the cut  $y$  axis in (c).

The geometry of the plasma was kept identical between the studied pulses with the outer strike point on the horizontal part of the outer target. The total outer target ion current,  $\Phi_{ot}$  in figure 2b, obtained by integrating the Langmuir probe measurements of the ion flux across the outer target, shows that the outer divertor ranged from high-recycling conditions to deep detachment during the density scan. The roll-over of the target ion current, indicating the onset of the detachment, took place early in the scan at approximately  $n_{e,edge} \approx 2.8 \times 10^{19} \text{ m}^{-3}$ . This was followed by deepening detachment, observed as decrease of  $\Phi_{ot}$  down to approximately 20% of its peak value with increasing  $n_{e,edge}$  before the density limit was reached.

### 3.2. EDGE2D-EIRENE density scan

An unseeded density scan was run with EDGE2D-EIRENE by varying the separatrix electron density at the outer midplane within  $n_{e,sep,omp} = 1.2 - 2.5 \times 10^{19} \text{ m}^{-3}$  by feedback fuelling. The radial transport coefficients for anomalous particle diffusion and heat conduction were kept constant throughout the scan, and cross-field drifts were activated. An input power of  $P_{in} = 2.0 \text{ MW}$ , divided equally between electrons and ions, was applied across the core boundary. The constant input power does not account for the increase in the contribution of Ohmic heating with the plasma density but corresponds to an approximative average over the experimental density scan. Parallel density scans with the input power varied within  $P_{in} = 1.0 - 3.0 \text{ MW}$  were also run, but the observed qualitative trends were similar with only quantitative differences. Therefore, the presented results concentrate on the  $P_{in} = 2.0 \text{ MW}$  scan.

The plasma geometry used in the EDGE2D-EIRENE simulations was similar to the studied experimental pulses with the simulation grid based on pulse 81472 which belonged to the precursor of the same experiment [60]. As seen in figure 2c, the outer divertor ranged from high-recycling to detached conditions during the density scan but did not reach as deep detachment as in the experiment due to numerical instabilities preventing further increase of the plasma density. However, the achieved set of divertor conditions is sufficient for the purposes of this work. It is emphasized that there was no aim to quantitatively match the simulations with the experiments but only to provide qualitative references for the behaviour of the divertor conditions within the experimentally relevant input parameter range.

## 4. Evolution of local outer divertor conditions during detachment

A key benefit of the camera-based methodology with respect to the established line-integrated spectroscopic measurements is the improved capability of localizing the observations of the plasma conditions in 2D. Consequently, distortions due to line integration — whose potential significance has been discussed in [9, 6] — are avoided and closer comparability to divertor plasma simulations is enabled.

### 4.1. Experimentally resolved divertor conditions in 2D

The tomographic reconstructions in figure 3 demonstrate the Balmer line emission distributions extending from strongly localized bright emission near the strike point to above the X-point, as the outer divertor proceeds from high-recycling conditions to deep de-

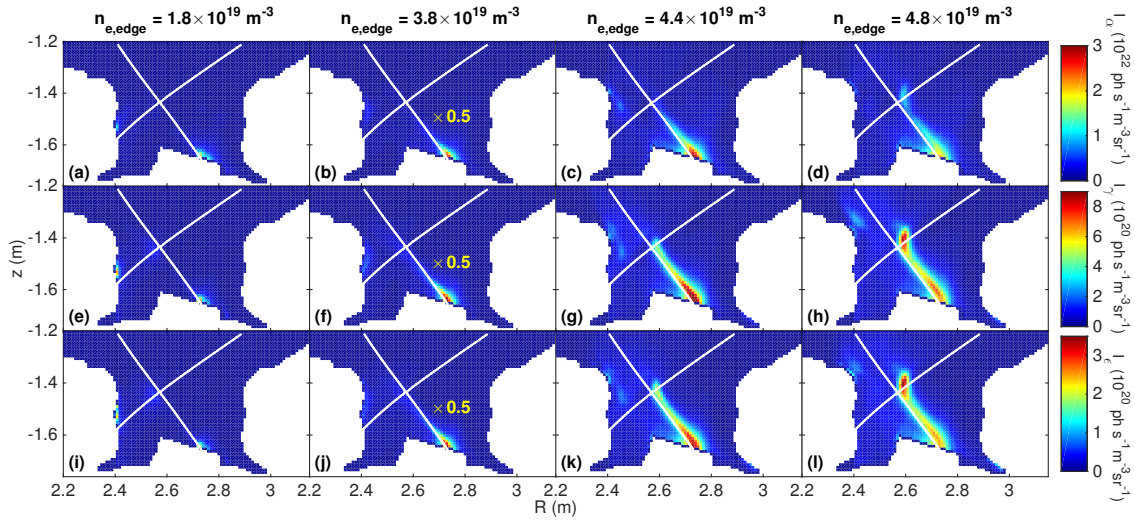


**Figure 3.** Tomographic reconstructions of the camera images of Balmer  $D_\alpha$  (a–d),  $D_\gamma$  (e–h) and  $D_\epsilon$  (i–l) emission show qualitative differences between the different lines, as their emission distributions extend from the outer strike point to above the X-point with increasing upstream density. In (b,f,j), the emission intensities have been scaled by a factor of 0.5 for improved consistency of the colour scales between the different density steps.

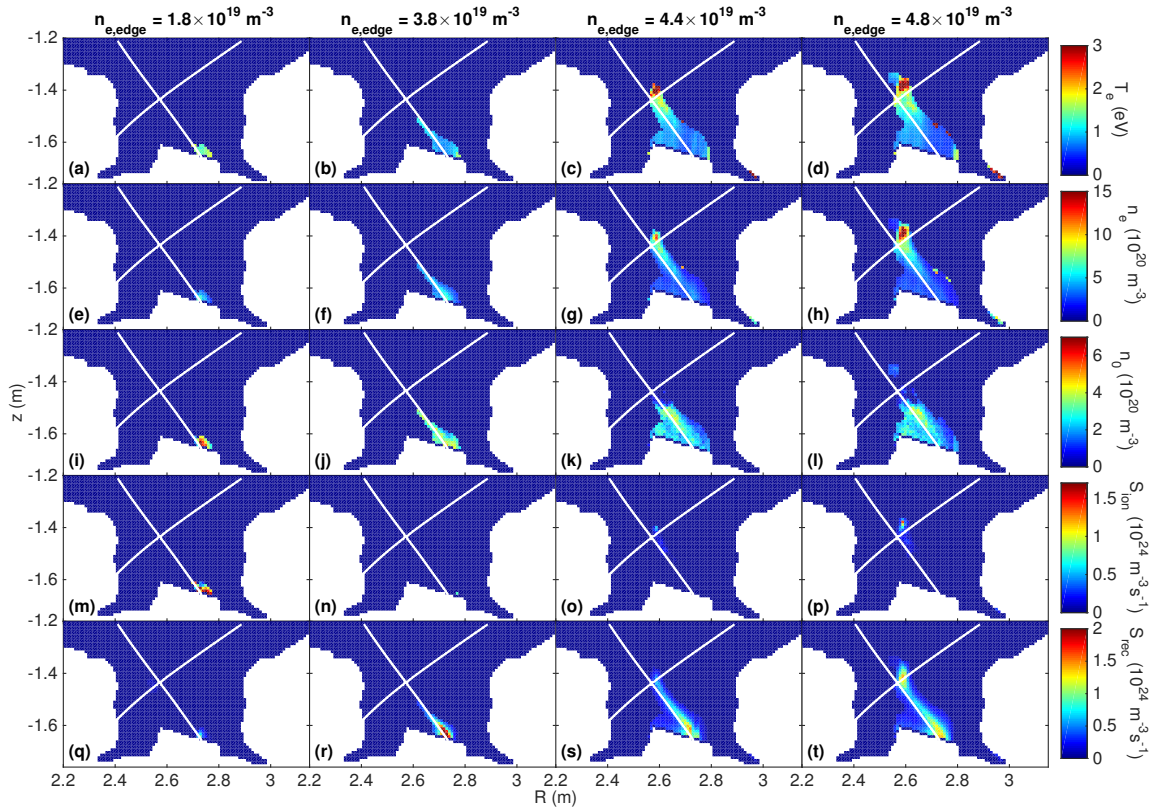


**Figure 4.** Experimentally resolved 2D estimates suggest the divertor temperature decreasing to  $T_e = 0.5 - 1.0$  eV in the outer divertor volume during detachment (a–d) and the high- $n_e$  region shifting from the outer strike point to above the X-point (f–h), while deuterium atoms primarily remain below the X-point (i–l). Ionization (m–p) is observed only at the outer strike point in high-recycling conditions (m) and above the X-point at the highest upstream densities (p), whereas volumetric recombination is seen extending continuously from the strike point to the X-point (q–t).

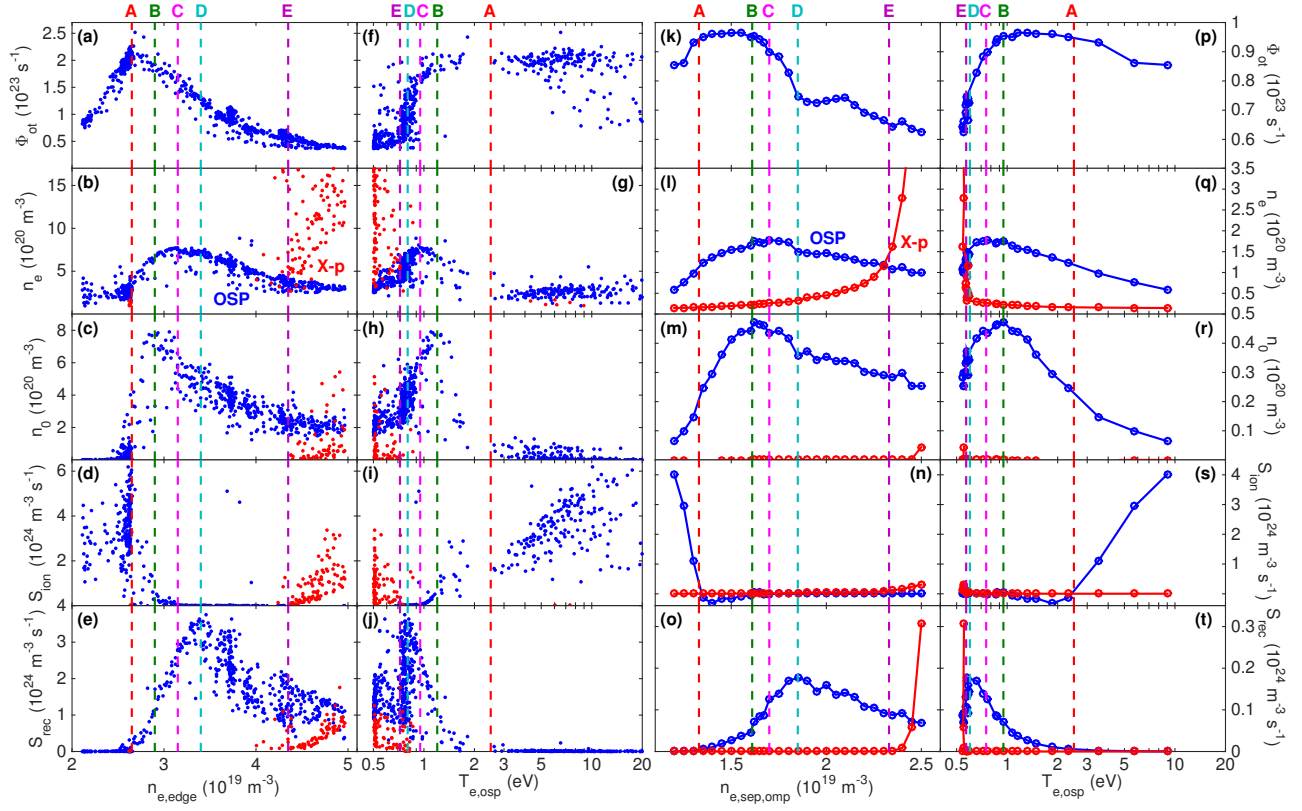


**Figure 5.** Experimentally estimated outer strike point conditions (OSP, blue) as functions of the upstream edge density (a–e) and strike point temperature (f–j) show qualitatively similar behaviour during detachment as EDGE2D-EIRENE predictions as functions of the outer midplane separatrix density (k–o) and  $T_{e,osp}$  (p–t). At the end of the density scans, both analyses show increase of  $n_e$  (b, g, l, q),  $n_0$  (c, h, m, r),  $S_{ion}$  (d, i, n, s) and  $S_{rec}$  (e, j, o, t) also above the X-point (X-p, red). The coloured vertical dashed lines indicate stages A–E in the sequence of events during detachment, as discussed in the text. Note the different scales between the experimental estimates (a–j) and the EDGE2D-EIRENE predictions (k–t) and the logarithmic  $x$  axes in (f–j) and (p–t).

tachment. In addition to elongation of the emission distribution, especially the strongly recombination-dominated  $D_\epsilon$  emission shows a shift of the brightest emission region from the vicinity of the outer strike point to the X-point region. The  $D_\alpha$  emission, instead, retains its strongest intensity near the strike point throughout the density scan. This can partially be attributed to the more pronounced excitation component in equation (1) but may also indicate emission contribution arising from molecular processes which affect  $D_\alpha$  the most. Line-integrated divertor spectroscopy showed no evidence of emission pollution from neighbouring impurity lines and indicated background continuum contribution below 5% for all studied camera filter ranges, suggesting good representation of the Balmer line emission by the camera data.

Solving equation (2) with the emission distributions of figure 3 indicates decrease of the outer divertor electron temperature to  $T_e \approx 0.5 - 1.0$  eV with deepening detachment in figures 4a–d, while the outer divertor high- $n_e$  region moves upstream from the outer strike point, eventually reaching values at  $n_e \approx 1.5 \times 10^{21} \text{ m}^{-3}$  above the X-point in figures 4e–

h. The  $T_e$  and  $n_e$  estimates were constrained with the help of line-integrated spectroscopic measurements and were found to reproduce the spectroscopically measured values within 20% when post-processed with synthetic spectroscopy, as discussed in [9]. Simultaneously, the atomic neutral density distribution in figures 4i–l spreads upstream and into the private flux region but mainly remains below the X-point. Applying the solutions for  $T_e$ ,  $n_e$  and  $n_0$  with equation (3) yields strong ionization rates at the outer strike point and the X-point at the lowest and highest upstream densities in figures 4m and p, respectively. The recombination rate, given by equation (4), shows a smoother transition from strong peaking at the outer target at the onset of detachment to an elongated distribution with a secondary peak above the X-point in deep detachment in figures 4q–t.

#### 4.2. Sequence of detachment at outer strike point

The experimentally resolved plasma conditions at the outer strike point were observed to agree qualitatively with the EDGE2D-EIRENE simulations,

showing similar trends and sequence of events, as the outer divertor proceeds from high-recycling to deeply detached conditions. In figure 5, the divertor conditions are investigated as functions of the upstream electron density as a common control parameter, as well as the outer strike point electron temperature for a more divertor-relevant visualization.

For the experimental data in figures 5a–e, the upstream edge density,  $n_{e,edge}$ , is given by the line-integrated interferometer measurement of the pedestal density at the outer midplane, whereas the feedback-controlled separatrix density at the outer midplane was used directly for the EDGE2D-EIRENE results in figures 5k–o. Due to the unreliability of the Langmuir probe measurements of  $T_e$  at detachment-relevant low temperatures and the relatively strong potential effect of line integration in the line-integrated spectroscopic  $T_e$  measurements at the lowest end of the observed  $T_e$  range, as discussed in [9], independent measurements for the outer strike point temperature,  $T_{e,osp}$ , were not available. Instead, figures 5f–j utilize the local  $T_{e,osp}$  obtained from the analysis presented in this work and in [9]. It is thus acknowledged that the  $T_{e,osp}$  axis may be affected by the uncertainties of the analysis.

The detachment process at the outer strike point is investigated in terms of increasing upstream density and decreasing strike point temperature. To compare the sequence of events during detachment between the experimental estimates and the simulation results, the evolution of the strike point conditions is discussed in stages, identified with points A–E in figure 5. The strike point temperatures referred to in the discussion are taken from the experimental analysis and agree with the corresponding EDGE2D-EIRENE predictions within the 25% error estimate of the experimentally resolved  $T_{e,osp}$ .

*Decrease of  $S_{ion}$  and onset of detachment ( $\rightarrow A$ ):* The transition from high-recycling conditions to the onset of detachment begins with a strong decrease in  $S_{ion}$  at the outer strike point before the target ion current,  $\Phi_{ot}$ , in figures 5a, f, k and p reaches its peak at  $T_{osp} \approx 2.5$  eV. This is observed in agreement between the experimental data in figures 5d and i and the EDGE2D-EIRENE predictions in figures 5n and s. In this phase, the experimental data in figures 5b, g, c and h show little variation in the strike point  $n_e$  and  $n_0$ , while an increase in both of them is predicted by EDGE2D-EIRENE. This can be attributed to the experimental analysis being challenged by the low emission intensities at low electron densities. At this stage, both analyses expectedly indicate almost total lack  $S_{rec}$  in figures 5e, j, o and t.

*Increase of  $n_e$ , increase and peaking of  $n_0$  ( $A \rightarrow B$ ):* As the outer strike point temperature falls below approximately  $T_{e,osp} \approx 2$  eV,  $\Phi_{ot}$  plateaus at its peak, while the strike point  $n_e$  and  $n_0$  increase steeply. At  $T_{e,osp} \approx 1.2$  eV, the strike point  $n_0$  reaches its maximum in both the experimental estimates and the EDGE2D-EIRENE predictions, while  $n_e$  keeps increasing. While the experimental observations and the simulations are not compared quantitatively, it is noted that the experimentally estimated values of  $n_0$  are significantly higher with respect to  $n_e$  than in the simulations. This may indicate overestimation due to the additional  $D_\alpha$  emission contribution arising from molecular processes and Lyman-series opacity, as discussed in section 2.4. At this stage, increase in also  $S_{rec}$  emerges in both analyses.

*Roll-over of  $\Phi_{ot}$ , increase of  $S_{rec}$ , peaking of  $n_e$  ( $B \rightarrow C$ ):* In both the experimental estimates and the EDGE2D-EIRENE simulations, the peaking of the strike point  $n_0$  coincides with  $\Phi_{ot}$  rolling over and starting to decrease, as the divertor enters detachment. While both analyses show  $n_0$  decreasing, the strike point  $n_e$  still increases beyond the roll-over of  $\Phi_{ot}$  before peaking at  $T_{e,osp} \approx 1.0$  eV.  $S_{rec}$  is observed to increase steeply throughout this stage in both experiments and modelling.

*Decrease of  $\Phi_{ot}$ , peaking of  $S_{rec}$  ( $C \rightarrow D$ ):* After the peaking of the strike point  $n_e$ ,  $\Phi_{ot}$  and  $n_0$  are observed to decrease steeply with decreasing  $T_{e,osp}$  in experiments and modelling.  $S_{rec}$  continues to increase, until the decreasing strike point  $n_e$  eventually halts the ascent at  $T_{e,osp} \approx 0.8$  eV.

*Roll-over of  $S_{rec}$  and deep detachment ( $D \rightarrow E$ ):* Below  $T_{e,osp} \approx 0.8$  eV, the decrease of the strike point  $n_e$  becomes more rapid, resulting in a drastic fall in  $S_{rec}$  across a narrow  $T_{e,osp}$  interval due to the  $n_e^2$  dependence in equation (4). Simultaneously, also  $\Phi_{ot}$  and  $n_0$  decrease steeply. It is noticeable that, despite only a minor change in  $T_{e,osp}$  between points D and E in figures 5f–j and p–t, reaching the deeply detached conditions requires a significant increase in the upstream density in figures 5a–e and k–o.

*Extension to above the X-point ( $E \rightarrow$ ):* Near the end of the density ramp with  $T_{e,osp} \approx 0.5 - 0.6$  eV and  $\Phi_{ot}$  at approximately 25% of its value at the roll-over point, the experimentally estimated strike point conditions are observed to plateau. The settling of the strike point conditions coincides with a strong emergence of experimentally resolved high  $n_e$  in the core plasma above the X-point together with increase in  $S_{ion}$  and  $S_{rec}$  and, to a lesser degree,  $n_0$  in the same region. At

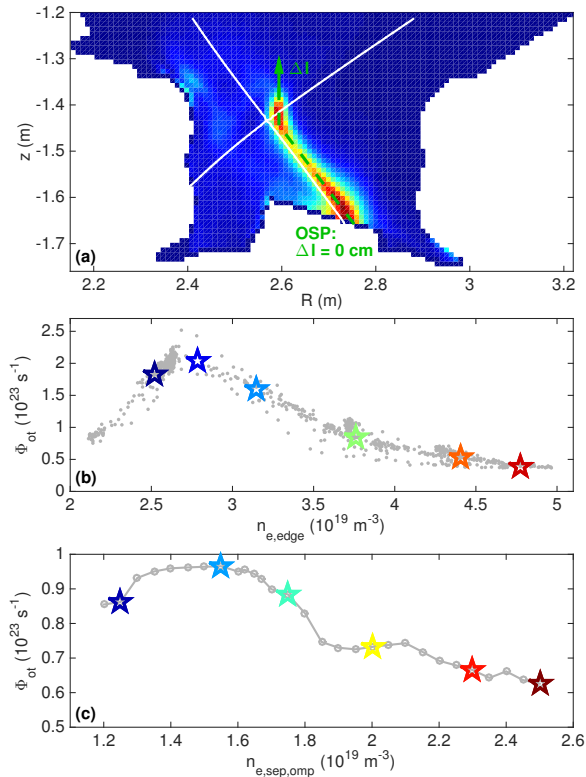


**Figure 6.** Evolution of the poloidal extent of the divertor conditions was investigated by tracing their 2D distributions from the outer strike point to above the X-point, as depicted by the green dashed arrow on top of the example  $D_e$  emission distribution (a). Examples for poloidal profiles were selected at different stages of the detachment process in the experimental (b) and EDGE2D-EIRENE (c) analyses, marked with stars on the respective roll-over curves of  $\Phi_{ot}$ . The colours of the stars derive from the upstream densities and correspond directly to the colours of the poloidal profiles in figure 7.

this stage, the electron temperature above the X-point was estimated at approximately  $T_e \approx 1.5\text{--}2.5$  eV in [9]. Plateauing of the strike point conditions at low  $T_{e,osp}$  is not observed in the EDGE2D-EIRENE simulations, but it is noted that the decrease of  $\Phi_{ot}$  in figure 5k does not suggest achievement of equally deep detachment as in the experiments. However, qualitatively similar increases in  $n_e$ ,  $n_0$ ,  $S_{ion}$  and  $S_{rec}$  above the X-point are observed also in the simulations, albeit the significantly stronger increase of  $S_{rec}$  suggests appearance of an X-point MARFE earlier in the simulations.

#### 4.3. Poloidal variation between outer strike point and X-point

The roll-overs of the divertor parameters and their eventual increase above the X-point are signs of their distributions extending upstream from the strike point, as the plasma cools down in the divertor volume with proceeding detachment. In addition to the 2D examples presented in figure 4, this extension has

been investigated by observing poloidal profiles of the divertor conditions, obtained by tracking their 2D distributions along the  $D_e$  emission region from the outer strike point to above the X-point, as visualized in figure 6a. The evolution of these poloidal profiles is demonstrated in figure 7 for both the experimental analysis and the EDGE2D-EIRENE simulations at different degrees of detachment, identified in figures 6b and c.

Gradual decrease of the divertor temperature from  $T_e \sim 10$  eV to  $T_e < 2.0$  eV everywhere between the outer strike point and the X-point during the deepening detachment is seen in the experimentally resolved poloidal profiles in figure 7a in agreement with the EDGE2D-EIRENE predictions in figure 7f. The differences in the poloidal lengths covered by the experimental profiles are due to the evolution in the spatial coverage of the Balmer line emission distributions with increasing upstream density.

At the lowest upstream densities,  $n_e$ ,  $n_0$  and  $S_{rec}$  show peaked poloidal profiles near the outer strike point in figures 7b, c and e, respectively. This is followed by flattening and extension of their distributions towards the X-point, as  $T_e$  decreases in the divertor volume with proceeding detachment, explaining the roll-over behaviour of these quantities at the outer strike point in figure 5. While a slight increase in  $n_0$  was observed also above the X-point at the highest upstream densities in figure 5c, figure 7c suggests that the majority of the atoms remains below the X-point at temperatures below  $T_e \approx 1.0$  eV. Instead, the  $n_e$  and  $S_{rec}$  profiles in figures 7b and e, respectively, show formation of distinct peaks above the X-point at high upstream densities, as observed previously also in figures 4 and 5. The shift of the density and recombination peaks in the poloidal profiles from the outer strike point to above the X-point is consistent with earlier experimental observations in, e.g., Alcator C-Mod [61, 62].

Qualitatively similar observations for the poloidal extension of the  $n_e$ ,  $n_0$  and  $S_{rec}$  distributions are made also for the EDGE2D-EIRENE simulations in figures 7g, h and j, respectively. For  $S_{ion}$ , however, the two analyses show different behaviours in figures 7d and i. Following the strong ionization source near the outer strike point at low upstream densities, practically no ionization is observed experimentally in the divertor volume above the roll-over density of  $n_{e,edge}^{roll-over} \approx 2.8 \times 10^{19} \text{ m}^{-3}$ , until a new peak emerges above the X-point at the highest densities. EDGE2D-EIRENE also predicts a strongly peaked  $S_{ion}$  distribution near the strike point at low upstream densities but, instead of complete lack of ionization, suggests gradual movement of the ionization front towards the X-point with increasing upstream density.

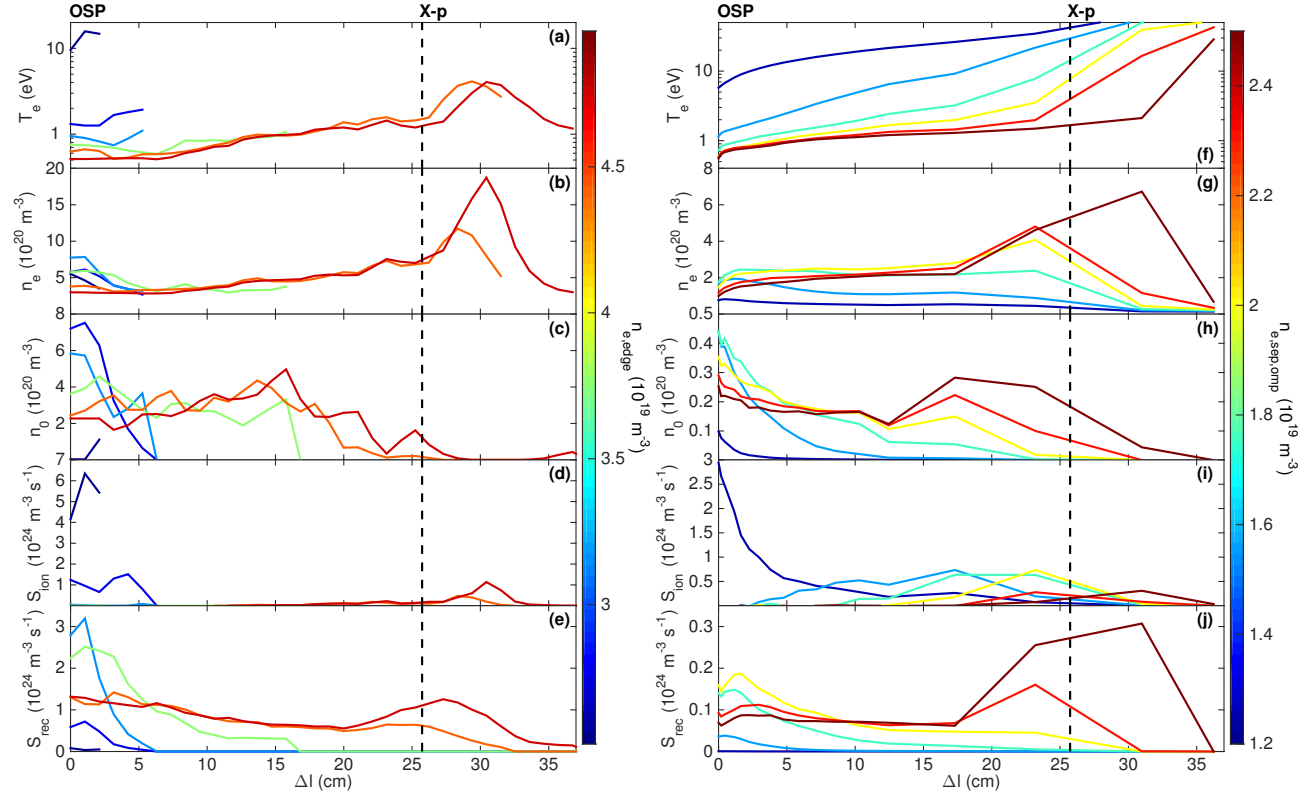


**Figure 7.** Poloidal profiles of the experimental estimates (a–e) and EDGE2D-EIRENE predictions (f–j) show decrease of the divertor temperature (a, f) from  $T_e = 10 - 20$  eV to below  $T_e = 2.0$  eV throughout the divertor volume during detachment, while  $n_e$  (b, g),  $n_0$  (c, h) and  $S_{\text{rec}}$  (e, j) evolve from peaked profiles near the outer strike point to flatter ones reaching the X-point. Ionization is observed only at the outer strike point and above the X-point at the lowest and highest upstream densities, respectively, in the experimental analysis (e) in contrast to the gradual shifting of the ionization front upstream in the EDGE2D-EIRENE simulations (j). The colours of the profiles are given by the upstream densities according to the provided colour bars and correspond to the different detachment stages identified in figures 6b and c. The coordinate  $\Delta l$  increases from the outer strike point ( $\Delta l = 0$  cm) to above the X-point along the path presented in figure 6a. The vertical dashed line marks the position of the X-point. Note the logarithmic  $T_e$  axes in (a, f) and the different scales between the experimental estimates (a–e) and the EDGE2D-EIRENE predictions (f–j).

This qualitative discrepancy is attributed mainly to the spatial restrictions of the experimental analysis and is discussed in more detail in section 5.3.

## 5. Global divertor conditions and particle balance

In addition to the local investigation of the outer strike point conditions, the experimental estimates were compared to the EDGE2D-EIRENE predictions also by integrating them over the entire outer divertor volume. The spatially wider examination enables assessing the physical credibility of the experimental analysis also in terms of, e.g., particle balance.

### 5.1. Evolution of global conditions across outer divertor volume

The volume integrals  $N_e = \int n_e dV_{\text{div}}$ ,  $N_0 = \int n_0 dV_{\text{div}}$ , and  $R_{\text{rec}} = \int S_{\text{rec}} dV_{\text{div}}$  of the experimentally estimated

divertor conditions show increase with varying rates with increasing upstream density in figures 8b, c and e. The observed behaviour is mostly in qualitative agreement with the EDGE2D-EIRENE predictions in figures 8l, m and o.

As  $\Phi_{\text{ot}}$  reaches its peak (point A) in the beginning of the density scan in 8a,  $N_e$  and  $N_0$  begin increasing rapidly in figures 8b and c, respectively, in agreement with the EDGE2D-EIRENE predictions in figures 8l and m. In both analyses,  $R_{\text{rec}}$  begins increasing slightly later, near the roll-over of  $\Phi_{\text{ot}}$ .

After the roll-over of  $\Phi_{\text{ot}}$  (point B), the increase of the experimentally resolved  $N_e$  and  $N_0$  plateaus, while  $R_{\text{rec}}$  keeps increasing and  $\Phi_{\text{ot}}$  decreasing with increasing  $n_{e,\text{edge}}$ . Similar plateauing of  $N_e$  and  $N_0$  is observed in the EDGE2D-EIRENE simulations, but also  $R_{\text{rec}}$  in figure 8o shows similar behaviour, flattening the decrease in  $\Phi_{\text{ot}}$  in figure 8k.

As the outer divertor proceeds to deeper detach-

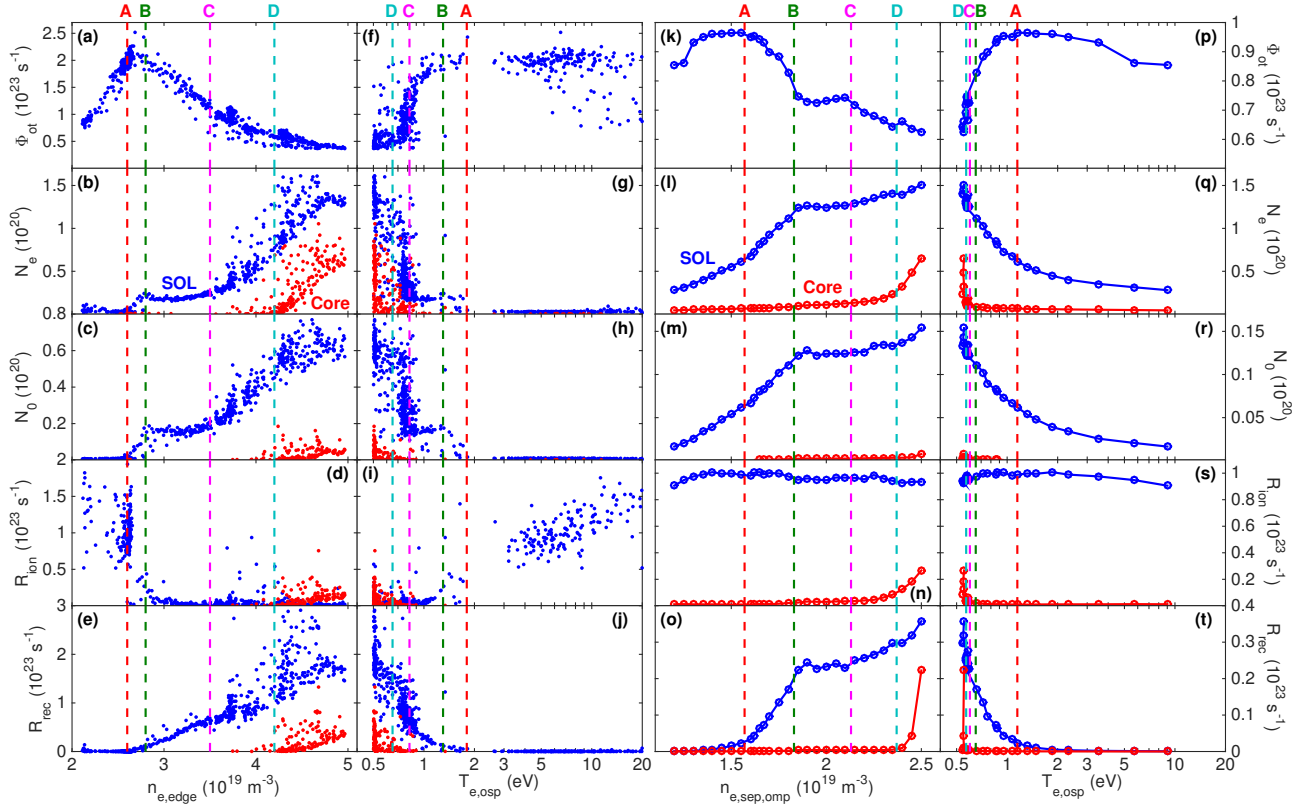


**Figure 8.** Volume integrals of the divertor conditions given by the experimental estimates (a–j) and EDGE2D-EIRENE predictions (k–t) as functions of the upstream density (a–e, k–o) and  $T_{e,osp}$  (f–j, p–t) agree qualitatively on the total numbers of electrons (b, g, l, q), atoms (c, h, m, r) and recombination events (e, j, o, t) increasing with upstream density in the outer divertor SOL (blue). After the roll-over of  $\Phi_{ot}$  (a, f), no ionization is observed in the divertor SOL in the experimental analysis (d, i) in contrast to the total ionization rate remaining relatively high throughout the density scan in the EDGE2D-EIRENE simulations (n, s). Both analyses show increase of  $N_e$ ,  $N_0$ ,  $R_{ion}$  and  $R_{rec}$  in the core volume above the X-point (red) at the highest upstream densities. The coloured vertical dashed lines indicate stages A–D in the evolution of the volume-integrated divertor conditions, as discussed in the text. These stages are different from the ones used in discussion of figure 5. Note the different scales between the experimental estimates (a–j) and the EDGE2D-EIRENE predictions (k–t) and the logarithmic  $x$  axes in (f–j) and (p–t).

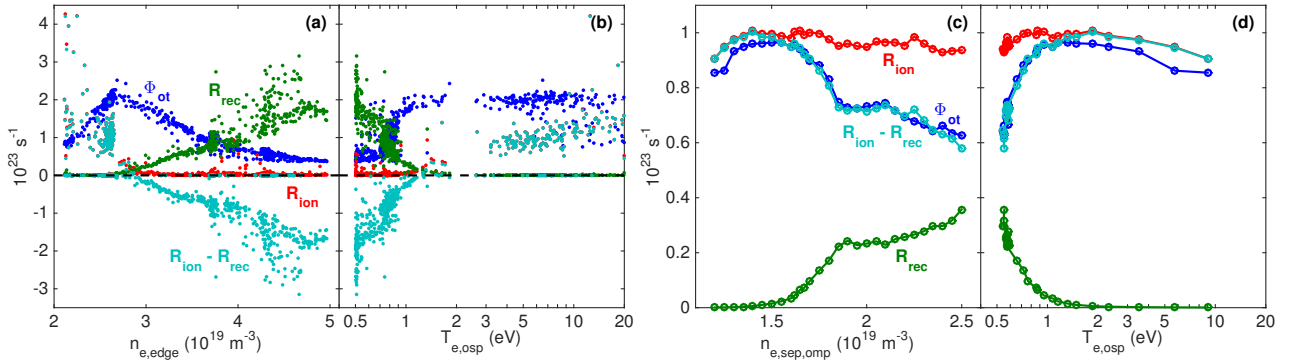


**Figure 9.** Shortfall in the experimentally observed ionization (red) in the outer divertor volume and the increase in recombination (green) lead to a significant discrepancy between  $\Phi_{ot}$  (blue) and  $R_{ion} - R_{rec}$  (cyan) and negative values of the latter above the roll-over density (a) with  $T_{e,osp} \leq 1.0$  eV (b). In the EDGE2D-EIRENE simulations (c, d), a similar investigation satisfies the particle balance within 10%. Note the logarithmic  $x$  axes in (b,d).

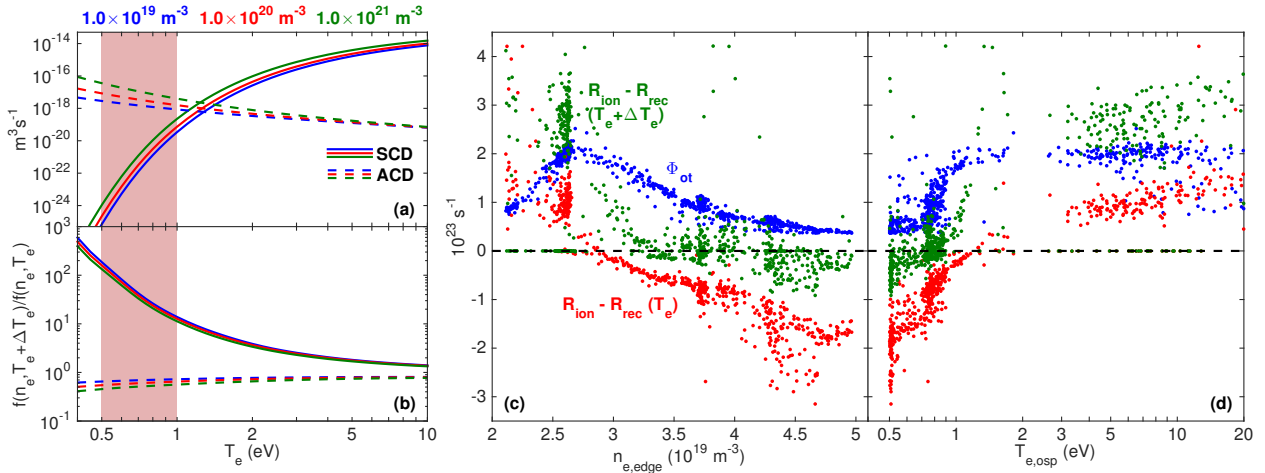


**Figure 10.** ADAS ionization rate coefficient  $SCD(n_e, T_e)$  (a, solid) shows strong variation within 4–5 orders of magnitude at low temperatures of  $T_e = 0.5 - 1.0$  eV (red shaded region), while less significant variation within an order of magnitude is observed for the ADAS recombination rate coefficient  $ACD(n_e, T_e)$  (a, dashed). Consequently, the addition of the 25%  $\Delta T_e$  in equations (3) and (4) leads to an increase of  $S_{ion}$  (b, solid) and decrease of  $S_{rec}$  (b, dashed) by factors of 10–200 and 2–3, respectively. Accounting for the error estimates in the investigation of the particle balance (c, d) narrows the difference between  $R_{ion} - R_{rec}$  (green) and  $\Phi_{ot}$  (blue) with respect to the previously presented curve (red) but is not sufficient to satisfy the particle balance at low temperatures. Note the logarithmic  $y$  axes in (a, b) and  $x$  axes in (a,b,d).

ment, with figure 7a showing a decrease in  $T_e$  to  $T_e \approx 1.0 - 1.5$  eV in most of the divertor volume, the aforementioned plateauing ends (point C), and steep increase is again observed for  $N_e$ ,  $N_0$  and  $R_{rec}$  with increasing  $n_{e,edge}$ . Similar ascent is seen also in the EDGE2D-EIRENE predictions, albeit with a noticeably shallower slope with increasing  $n_{e,sep,omp}$  than before the plateauing. As already discussed in connection to figures 5 and 7, both analyses show  $N_e$ ,  $N_0$  and  $R_{rec}$  increasing also in the core volume above the X-point at the highest upstream densities (point D).

Despite the reasonable qualitative agreement between the experimental estimates and EDGE2D-EIRENE predictions for  $N_e$ ,  $N_0$  and  $R_{rec}$ , stark differences are seen for the volume-integrated ionization rate  $R_{ion} = \int S_{ion} dV_{div}$ , as already suggested by figure 7. The behaviour of the experimentally resolved  $R_{ion}$  in figure 8d resembles that of the local  $S_{ion}$  at the outer strike point in figure 5d, showing steep decrease in the beginning of the density scan and virtually no ionization in the divertor volume beyond the roll-over of  $\Phi_{ot}$ . Instead,  $R_{ion}$  shows only slight decrease above the roll-over density in the EDGE2D-EIRENE simulations and remains almost at the same level as before the roll-over in figure 8n. As discussed already in sections 4.2 and 4.3, both analyses agree on increase of ionization in the core volume above the X-point near the end of the density scan.

## 5.2. Ionization shortfall and particle balance

The shortfall in the experimentally resolved  $R_{ion}$  discussed above is directly reflected on the fulfilment of the approximative particle balance

$$\Phi_{ot} \approx R_{ion} - R_{rec} \quad (5)$$

in the outer divertor. Here, the volumetric ionization and recombination events are assumed to dominate the target ion flux over the  $D^+$  ion transport into and out of the outer divertor. Figures 9a and b show the experimentally derived  $R_{ion} - R_{rec}$  agreeing with  $\Phi_{ot}$  within a factor of 2 only in the beginning of the density scan before the roll-over of  $\Phi_{ot}$  with  $T_{e,osp} > 3.0$  eV. At the onset of detachment, the steep decrease of  $R_{ion}$  makes  $R_{ion} - R_{rec}$  fall rapidly towards zero and eventually to negative values due to the increasing  $R_{rec}$  at  $T_{e,osp} \leq 1.0$  eV, thus terminating the validity of equation (5). In the EDGE2D-EIRENE simulations, close agreement between  $R_{ion} - R_{rec}$  and  $\Phi_{ot}$  within 10% is observed throughout the density scan in figures 9c and d.

The strong deviations in the experimentally inferred particle balance can partially be attributed to the ADAS ionization rate coefficient  $SCD(n_e, T_e)$  in equation (3) varying steeply by 4–5 orders of magnitude within the temperature range of  $T_e = 0.5 - 1.0$  eV, as visualized in figure 10a. Consequently, figure 10b shows the addition of the 25% error estimate of  $T_e$  leading to an increase of the calculated  $S_{ion}$  by a factor of 10–200 at the lowest temperatures. Simultaneously,  $S_{rec}$  decreases less noticeably by a factor of 2–3 due to the effect of the increased  $T_e$  on  $ACD(n_e, T_e)$  in

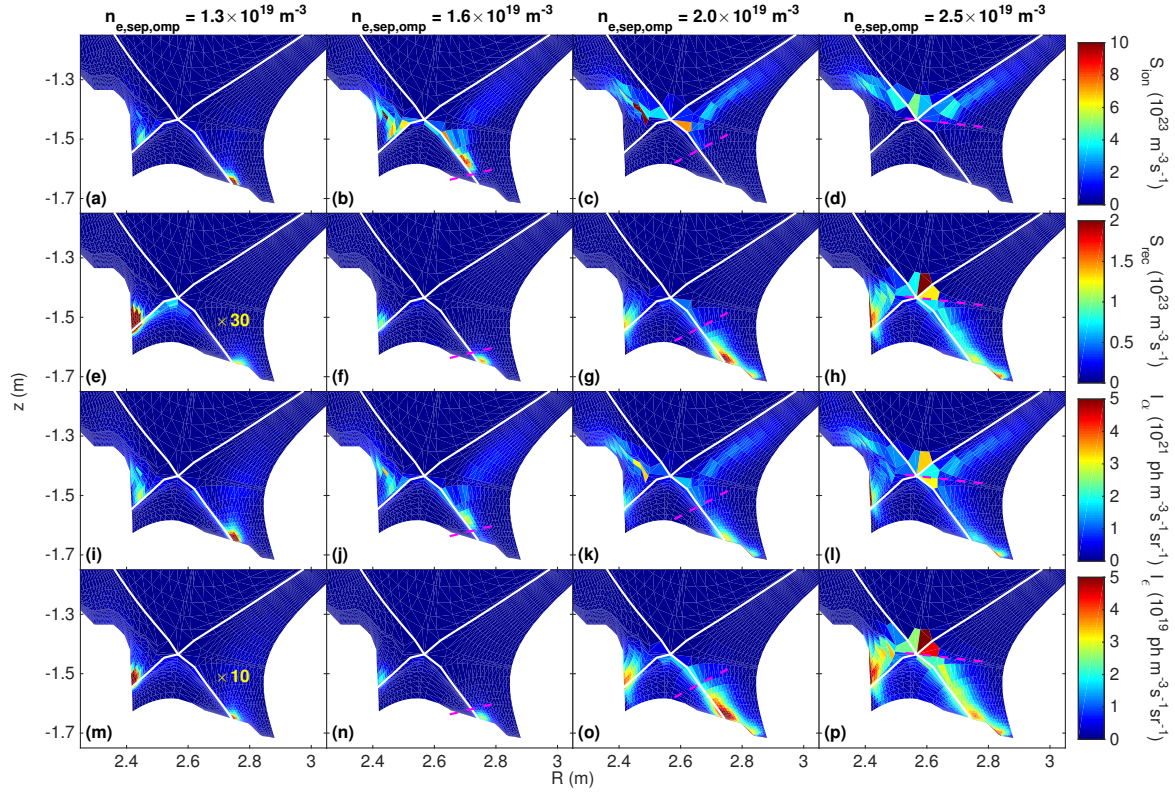


**Figure 11.** EDGE2D-EIRENE simulations show the ionization front in the outer divertor SOL shifting from the strike point upstream to above the vertical level of the X-point with proceeding detachment (a–d), while the recombination region remains closer to the target with minimal spatial overlap with the ionization front above the roll-over density (e–h). Consequently, the  $D_\alpha$  emission distribution extends widely upstream from the outer strike point region (i–l), whereas the  $D_\epsilon$  emission remains primarily below the X-point (m–p). The magenta dashed lines mark roughly the low end of vertical span of the ionization front. The recombination rate in (e) and the  $D_\epsilon$  emission in (m) are scaled by factors of 30 and 10, respectively, for improved consistency of the colour scales.

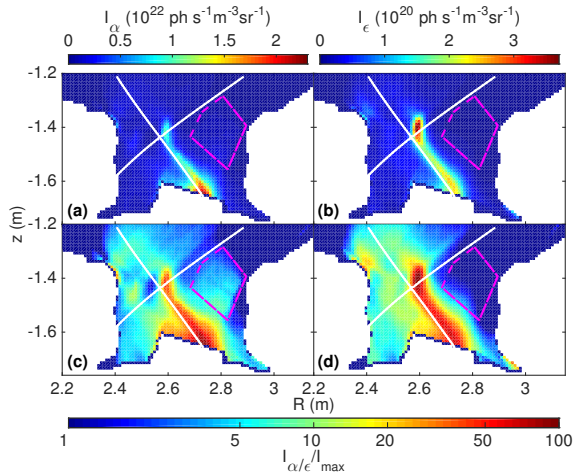


**Figure 12.** Tomographic reconstructions show signs of possible ionization-related weak extension of the  $D_\alpha$  emission distribution (a, c) in the upper part of the outer divertor, framed with the magenta dashed lines. Recombination-dominated  $D_\epsilon$  emission is not observed in the same region (b, d). Note the logarithmic colour scale in (c, d).

equation (4). While the consideration of  $\Delta T_e$ , as well as  $\Delta n_e$  and  $\Delta n_0$  with less significant effects on  $S_{\text{ion}}$ , narrows the difference between  $R_{\text{ion}} - R_{\text{rec}}$  and  $\Phi_{\text{ot}}$ , the particle balance remains mainly negative at the lowest temperatures, failing to satisfy equation (5). Hence, the susceptibility of  $SCD(n_e, T_e)$  to small variations in  $T_e$  at low temperatures can be concluded to severely complicate quantitative determination of  $S_{\text{ion}}$  but not fully account for the invalid particle balance. Due to the order of magnitude of the ionization shortfall, the effect of Lyman opacity on  $SCD$  and  $ACD$ , discussed in [6], is not believed to be the primary reason for the mismatch either.

### 5.3. Spatial restrictions in observing the ionization front

As discussed in section 2.4, the reliance on the  $D_\epsilon$  emission restricts the applicability of the methodology used in this work to high-recycling and detached divertors with sufficiently strong contributions from recombination to yield prominent  $D_\epsilon$  radiation. In such conditions, complete observation of  $S_{\text{ion}}$  is not

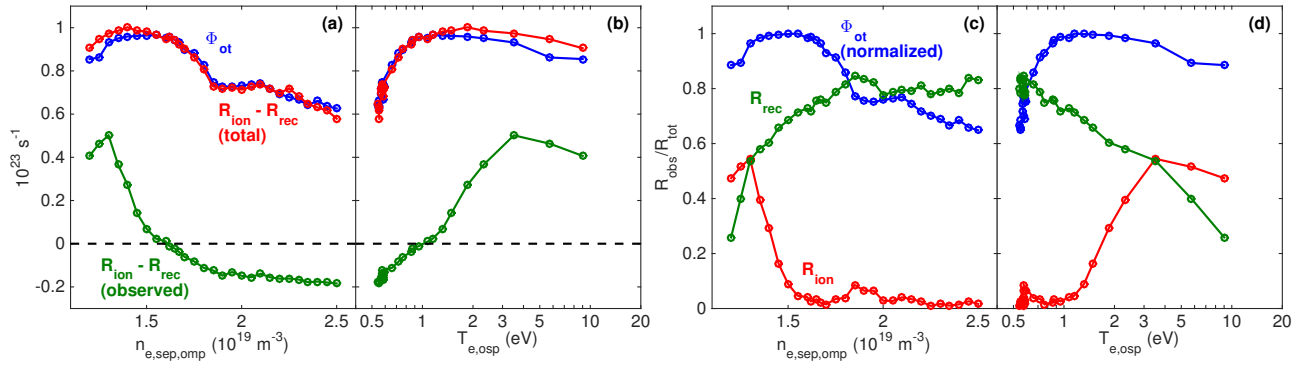


**Figure 13.** While  $R_{\text{ion}} - R_{\text{rec}}$  integrated over the entire outer divertor SOL (red) agrees within 10% with  $\Phi_{\text{ot}}$  (blue) in the EDGE2D-EIRENE simulations, considering only ionization and recombination observed within the  $D_{\varepsilon}$  emission region (green) yields similar discrepancies in the particle balance as in the experimental studies (a, b). The ratios of the numbers of ionization and recombination events within the  $D_{\varepsilon}$  emission region and the entire divertor volume in the EDGE2D-EIRENE simulations suggest that up to 80% of the recombination (green) but almost none of the ionization (red) in the outer divertor volume can be accounted for by observing  $D_{\varepsilon}$  emission in detached conditions (c, d). The roll-over curve of  $\Phi_{\text{ot}}$  in (c, d) is normalized to its maximum value and presented as a guideline for the detachment process. Note the logarithmic  $x$  axes in (b,d).

guaranteed due to the ionization and recombination concentrating partially or fully in different regions in the divertor volume.

The EDGE2D-EIRENE simulations show movement of the ionization front in the outer divertor SOL upstream from the vicinity of the outer strike point to above the level of the X-point with increasing upstream density in figures 11a–d. Simultaneously, apart from the high-recycling conditions at the lowest upstream densities, the recombination region extends towards the X-point in figures 11e–h but remains spatially below the ionization front with minimal overlap between the two. This is also reflected in the corresponding  $D_{\alpha}$  and  $D_{\varepsilon}$  emission distributions in figures 11i–l and m–p, respectively. The  $D_{\alpha}$  emission remains bright near the outer target due to the recombination component in equation (1) but also extends poloidally upstream from the X-point along with the ionization front due to the excitation component. The recombination-dominated  $D_{\varepsilon}$  emission, instead, remains below the X-point in accordance with the recombination region. Signs of similar behaviour are observed also in the experimental tomographic reconstructions in figure 12, where the  $D_{\alpha}$  emission shows a relatively weak wing-like extension upstream into a region where  $D_{\varepsilon}$  emission is not seen.

The lack of spatial overlap between the  $D_{\varepsilon}$  and  $S_{\text{ion}}$  distributions in figure 11 indicates strong limitations in observing ionization with the presented methodology, explaining the failure to satisfy the experimental particle balance in figure 9. This is supported by figures 13a and b in which the  $R_{\text{ion}} - R_{\text{rec}}$  of figures 9c and d have been re-calculated, taking into account only the ionization and recombination within the  $D_{\varepsilon}$  emission region. As observed in the experimental analysis,  $R_{\text{ion}} - R_{\text{rec}}$  decreases to

noticeably lower values than  $\Phi_{\text{ot}}$  and becomes negative in the detached conditions at  $T_{e,\text{osp}} < 1.0$  eV. The shift of the ionization front to beyond the extent of the  $D_{\varepsilon}$  emission region is further highlighted in figures 13c and d, where the share of the outer divertor ionization taking place within the  $D_{\varepsilon}$  emission region decreases steeply to below 5% in detachment. Simultaneously, the simulations show 70–80% of recombination in the outer divertor volume coinciding spatially with the  $D_{\varepsilon}$  emission region, when  $T_{e,\text{osp}} < 1.0$  eV.

The observations described above suggest that the presented methodology is viable for investigating the role of volumetric recombination in the detachment process. However, the failure to fulfil the particle balance experimentally, together with the EDGE2D-EIRENE predictions of the spatial evolution of the  $S_{\text{ion}}$  and  $S_{\text{rec}}$  distributions, indicates that quantitative studies of the ionization front are not possible above the roll-over density due to its lack of spatial overlap with the  $D_{\varepsilon}$  emission region. Instead, conclusions can primarily be drawn only on the lower vertical limit above which the ionization front has shifted.

## 6. Conclusions

Evolution of local  $T_e$ ,  $n_e$ ,  $n_0$ ,  $S_{\text{ion}}$  and  $S_{\text{rec}}$  in the outer divertor were studied experimentally during progressing detachment in an L-mode density ramp in JET-ILW. Quantitative 2D estimates for the divertor conditions were derived from tomographic reconstructions of divertor camera measurements of the deuterium Balmer line emission by expanding the methodology presented in [9] with further atomic data for calculation of the ionization and recombination rates. The experimental observations were compared

qualitatively to the results of an EDGE2D-EIRENE density scan with a roughly similar input parameter space as in the experiments.

The experimental analysis shows the detachment of the outer divertor beginning with a steep decrease of  $S_{\text{ion}}$  at the outer strike point, as the strike point temperature decreases to  $T_{\text{e,osp}} < 2.5$  eV. This is followed by strong increase and roll-over of first the strike point  $n_0$  at  $T_{\text{e,osp}} \approx 1.2$  eV, coinciding with roll-over of  $\Phi_{\text{ot}}$ , then  $n_e$  at  $T_{\text{e,osp}} \approx 1.0$  eV and finally in deep detachment  $S_{\text{rec}}$  at  $T_{\text{e,osp}} \approx 0.8$  eV, as the spatial distributions of the aforementioned quantities extend upstream from the outer strike point towards the X-point. Qualitatively similar behaviour with the same roll-over sequence of the strike point conditions is observed also in the EDGE2D-EIRENE simulations.

Integrated over the outer divertor volume, both the experimental analysis and the EDGE2D-EIRENE predictions show the total number of electrons, atoms and recombination events increasing with increasing upstream density with a plateau in the increase of  $N_e$  and  $N_0$  across a narrow upstream density range above the roll-over density. At the highest upstream densities, both analyses observe increase of  $n_e$ ,  $n_0$ ,  $S_{\text{ion}}$  and  $S_{\text{rec}}$  also in the core plasma above the X-point. The experimental methodology was, however, found unable to observe ionization in the divertor SOL after the roll-over of  $\Phi_{\text{ot}}$ , resulting in failure to satisfy the particle balance in outer divertor. This limitation is supported by the EDGE2D-EIRENE simulations which show the ionization front shifting rapidly upstream towards the outer midplane with no remaining spatial overlap with the recombination-dominated  $D_\epsilon$  emission region required for the analysis.

The qualitative consistency with the EDGE2D-EIRENE simulations suggests that spectroscopic divertor cameras can be utilized in expanding the established spectroscopic analysis of the divertor plasmas to obtain quantitative 2D estimates of  $T_e$ ,  $n_e$ ,  $n_0$  and  $S_{\text{rec}}$ . This improves the spatial comparability between experimental observations and divertor modelling and aids in localizing details which may otherwise be shadowed by the line integration effect of spectroscopic methods, as demonstrated in [9]. However, the reliance of the method on the recombination-dominated  $D_\epsilon$  emission limits its applicability to diagnosing plasma in or close to detached condition and severely restricts its spatial coverage and, consequently, ability to observe the evolving ionization front. Further dedicated studies are also still required to resolve the susceptibility of the method to the effects of Lyman opacity and Balmer line emission arising from molecular interactions.

## Acknowledgements

This work has been carried out within the framework of the EUROfusion Consortium and has received funding from the Euratom research and training programme 2014-2018 and 2019-2020 under grant agreement No 633053. The views and opinions expressed herein do not necessarily reflect those of the European Commission.

## References

- [1] SI Krasheninnikov et al 2016 *Physics of Plasmas* **23** 55602
- [2] AG Meigs et al 2000 *27th EPS Conference on Plasma Physics* 1264–1267
- [3] S Potzel et al 2014 *Plasma Physics and Controlled Fusion* **56** 025010
- [4] B Lomanowski et al 2015 *Nuclear Fusion* **55** 123028
- [5] D Lumma et al 1997 *Physics of Plasmas* **4** 2555
- [6] B Lomanowski et al 2020 *Plasma Physics and Controlled Fusion* **62** 065006
- [7] S Potzel et al 2014 *Nuclear Fusion* **54** 013001
- [8] K Verhaegh et al 2017 *Nuclear Materials and Energy* **12** 1112–1117
- [9] J Karhunen et al 2020 *Nuclear Materials and Energy* **25** 100831
- [10] B Lomanowski et al 2019 *Nuclear Materials and Energy* **20** 100676
- [11] J Karhunen et al 2019 *Review of Scientific Instruments* **90** 103504
- [12] K Itami et al 2001 *Journal of Nuclear Materials* **290–293** 633–638
- [13] A Huber et al 2003 *Journal of Nuclear Materials* **313–316** 925–930
- [14] A Huber et al 2012 *Review of Scientific Instruments* **83** 10D511
- [15] J Harrison et al 2011 *Journal of Nuclear Materials* **415** S379–S382
- [16] A Huber et al 2013 *Journal of Nuclear Materials* **438** S139–S147
- [17] ME Fenstermacher et al 1997 *Review of Scientific Instruments* **68** 974
- [18] ME Fenstermacher et al 1997 *Journal of Nuclear Materials* **241–243** 666–671
- [19] ME Fenstermacher et al 1999 *Journal of Nuclear Materials* **266–269** 348–353
- [20] CJ Boswell et al 2001 *Review of Scientific Instruments* **72** 935
- [21] BP Duval et al 1999 *Bulletin of American Physical Society* **44** GP175
- [22] J Harrison et al 2017 *Nuclear Materials and Energy* **12** 1071–1076
- [23] A Perek et al 2019 *Review of Scientific Instruments* **90** 123514
- [24] A Perek et al *Nuclear Materials and Energy* (submitted)
- [25] J Harhausen et al 2011 *Plasma Physics and Controlled Fusion* **53** 025002
- [26] M Odstrčil et al 2014 *Review of Scientific Instruments* **85** 013509
- [27] A Huber et al 2015 *Journal of Nuclear Materials* **463** 445–449
- [28] A Huber et al 2017 *Nuclear Fusion* **57** 086007
- [29] JL Terry et al 1998 *Physics of Plasmas* **5** 1759
- [30] B Lipschultz et al 1998 *Physics Review Letters* **81** 1007–1010
- [31] RC Isler et al 1997 *Physics of Plasmas* **4** 2989
- [32] K Fujimoto et al 2009 *Plasma and Fusion Research* **4** 025

- [33] M Agostini et al 2019 *Plasma Physics and Controlled Fusion* **61** 115001
- [34] C Bowman et al 2020 *Plasma Physics and Controlled Fusion* **62** 045014
- [35] R Simonini et al 1997 *Contributions to Plasma Physics* **34** 368
- [36] D Reiter et al 1992 *Journal of Nuclear Materials* **196–198** 80–89
- [37] S Wiesen 2006 *EDGE2D/EIRENE code interface report* JET ITC-Report, [www.eirene.de/e2deir\\_report\\_40jun06.pdf](http://www.eirene.de/e2deir_report_40jun06.pdf)
- [38] HP Summers 2004 *The ADAS User Manual, version 2.6*, <http://www.adas.ac.uk>
- [39] TM Biewer et al 2012 *Review of Scientific Instruments* **83** 10D505
- [40] V Huber et al 2016 *Review of Scientific Instruments* **87** 11D430
- [41] NJ Conway et al 2018 *Review of Scientific Instruments* **89** 10K107
- [42] M Carr et al 2019 *Review of Scientific Instruments* **90** 043504
- [43] S Silburn, A Meakins, T Farley 2019 *euratom-software/calcam: Calcam v2.4 (Version v2.4.0)*, <http://doi.org/10.5281/zenodo.3530201>
- [44] WK Hastings et al 1970 *Biometrika* **57** 97–109
- [45] A Patil et al 2010 *Journal of Statistical Software* **35** 1–81
- [46] AG Meigs et al 2010 *Review of Scientific Instruments* **81** 10E532
- [47] B Lomanowski et al 2014 *Review of Scientific Instruments* **85** 11E432
- [48] TN Carlstrom et al 1995 *Review of Scientific Instruments* **66** 493
- [49] F Glass et al 2016 *Review of Scientific Instruments* **87** 11E508
- [50] TN Carlstrom et al 2018 *Review of Scientific Instruments* **89** 10C111
- [51] CF Maggi et al 1999 *Journal of Nuclear Materials* **266–269** 867–872
- [52] V Kotov et al 2006 *Contributions to Plasma Physics* **46** 635–642
- [53] V Kotov et al 2006 *33rd EPS Conference on Plasma Physics* P–1.128
- [54] V Kotov et al 2007 *Numerical study of the ITER divertor plasma with the B2-EIRENE code package* Juel-4257
- [55] K Behringer et al 2000 *New Journal of Physics* **2** 23.1–23.19
- [56] M Groth et al 2019 *Nuclear Materials and Energy* **19** 211–217
- [57] S Menmuir et al 2007 *Journal of Quantitative Spectroscopy and Radiative Transfer* **105** 425–437
- [58] R Dey et al 2019 *Nuclear Fusion* **59** 076005
- [59] K Verhaegh et al 2021 *Plasma Physics and Controlled Fusion* **63** 035018
- [60] M Groth et al 2013 *Nuclear Fusion* **53** 093016
- [61] B Lipschultz et al 1999 *Journal of Nuclear Materials* **266–269** 370–375
- [62] B Lipschultz et al 1999 *Physics of Plasmas* **6** 1907–1916

## Appendix A. List of EDGE2D-EIRENE simulations

The EDGE2D-EIRENE simulations presented in this work comprise a density scan in which the separatrix density at the outer midplane,  $n_{e,sep,omp}$ , was varied within  $1.20 - 2.50 \times 10^{19} \text{ m}^{-3}$ , as specified in the first column of table A1, primarily in intervals of  $0.05 \times 10^{19} \text{ m}^{-3}$  with selected additional intermediate steps added for increased amount of data near the

roll-over point of  $\Phi_{ot}$ . To demonstrate the state of the outer divertor at each density step, the second and third columns of table A1 show the electron temperature at the outer strike point decreasing from  $T_{e,osp} = 9.0 \text{ eV}$  to  $T_{e,osp} = 0.55 \text{ eV}$ , while the outer divertor proceeds from high-recycling to detached conditions. The arrows in the third column indicate whether  $\Phi_{ot}$  is increasing with upstream density in high-recycling conditions ( $\uparrow$ ), peaking and rolling over ( $\curvearrowright$ ) or decreasing with deepening detachment ( $\downarrow$ ).

The simulation output has been stored on the JET analysis cluster in the EDGE2D-EIRENE catalogue. Each simulation case can be found in the catalogue under `jdkarh/edge2d/jet/81472/<DATE>/<SEQ#>`, where the place holders for the catalogue date, `<DATE>`, and sequence number, `<SEQ#>`, are replaced with the case-specific identifiers provided in the fourth and fifth columns of table A1. The reader is advised to consult the main author prior to accessing the data.

**Table A1.** The feedback-controlled separatrix electron density at the outer midplane was increase within  $n_{e,sep,omp} = 1.20 - 2.50 \times 10^{19} \text{ m}^{-3}$ , resulting in the outer strike point electron temperature decreasing from  $T_{e,osp} = 9.0 \text{ eV}$  to  $T_{e,osp} = 0.55 \text{ eV}$  and  $\Phi_{ot}$  first increasing ( $\uparrow$ ) in high-recycling conditions, peaking and rolling over ( $\curvearrowright$ ) and decreasing ( $\downarrow$ ) in detached conditions. The simulations can be accessed in the EDGE2D-EIRENE catalogue with the help of the specified identifiers for the catalogue date and sequence number.

$n_{e,sep,omp} (10^{19} \text{ m}^{-3})$	$T_{e,osp} \text{ (eV)}$	$\frac{\Phi_{ot}}{\Phi_{ot,max}} \text{ (\%)} \uparrow$	Date	Seq. #
1.20	9.01	88.5 ( $\uparrow$ )	jun3020	seq#1
1.25	5.75	89.3 ( $\uparrow$ )	aug2620	seq#1
1.30	3.51	96.5 ( $\uparrow$ )	jun3020	seq#2
1.35	2.32	98.4 ( $\uparrow$ )	aug2720	seq#1
1.40	1.85	99.4 ( $\curvearrowright$ )	jun3020	seq#3
1.45	1.49	99.6 ( $\curvearrowright$ )	aug2720	seq#2
1.50	1.32	99.8 ( $\curvearrowright$ )	jul0120	seq#2
1.55	1.15	100.0 ( $\curvearrowright$ )	aug2720	seq#3
1.60	1.08	98.4 ( $\curvearrowright$ )	jul0120	seq#3
1.62	0.95	98.9 ( $\curvearrowright$ )	aug2920	seq#7
1.65	0.87	97.6 ( $\downarrow$ )	aug2720	seq#4
1.67	0.85	96.3 ( $\downarrow$ )	aug3020	seq#1
1.70	0.77	93.1 ( $\downarrow$ )	jul0220	seq#3
1.75	0.72	91.5 ( $\downarrow$ )	aug2720	seq#5
1.80	0.66	85.9 ( $\downarrow$ )	jun2920	seq#1
1.85	0.58	77.3 ( $\downarrow$ )	aug2920	seq#10
1.90	0.57	75.6 ( $\downarrow$ )	jun3020	seq#4
1.95	0.59	75.1 ( $\downarrow$ )	aug3020	seq#3
2.00	0.59	75.8 ( $\downarrow$ )	jun2920	seq#2
2.05	0.59	76.4 ( $\downarrow$ )	aug2920	seq#11
2.10	0.57	76.9 ( $\downarrow$ )	jun2920	seq#3
2.15	0.57	74.4 ( $\downarrow$ )	aug3020	seq#4
2.20	0.57	71.7 ( $\downarrow$ )	jul0120	seq#4
2.25	0.58	70.3 ( $\downarrow$ )	aug3020	seq#5
2.30	0.58	68.9 ( $\downarrow$ )	jul0120	seq#5
2.35	0.55	66.6 ( $\downarrow$ )	aug3020	seq#6
2.40	0.55	68.5 ( $\downarrow$ )	jul0320	seq#3
2.45	0.55	65.9 ( $\downarrow$ )	sep0220	seq#4
2.50	0.55	64.8 ( $\downarrow$ )	jul0120	seq#6